PNAS
www.pnas.org

Supplementary Information for

Silver route to cuprate analogs

Jakub Gawraczyński et al.

This PDF file includes:

www.pnas.org/cgi/doi/10.1073/pnas.1812857116

Supporting Information Text

Five-band Hubbard model for AgF_2. As for cuprates(1), one can consider a simplified model of the electronic structure of AgF_2 in which the more relevant d and p orbitals are taken into account. Since accurate values of electronic parameters are not available for d^9 Ag compounds, our aim here is to provide estimates of the more important parameters that determine the magnetic interaction in AgF_2. In addition, we discuss the similarities and difference of the parameters with cuprates and show that a large value of the magnetic interaction in AgF_2 is compatible with the parameter estimates.

A natural choice for a minimal model, is to consider one $d_{x^2-y^2}$ orbital per Ag. For the F's, due to the strongest buckling with respect to cuprates, one should consider one extra p-orbital per fluorine atom which mixes significantly with the d-orbital. Figure S2 shows schematically a silver-fluorine-silver (L-F-R) bond and defines the more relevant orbitals. Here, L and R are left and right silver ions and F refers to the bridging fluoride. We call η the L-F-R angle. Orbitals are defined in the caption. In the room temperature structure(2) $\eta = 129.9^0$.

By symmetry, the $p_\perp$ orbital taken in the direction of the red arrow in Figure S2 has negligible mixing with the $d_{L/R}$ orbitals. Therefore, we restrict to two p orbitals for the central F, namely $p_\parallel$ parallel to the L-R line (green arrow) and p_z in the plane that contains the L-F-R triangle and perpendicular to the bond (blue arrow).

To model the AgF_2 electronic structure, since there are two fluorine atoms per f.u. one should consider a five-band Hubbard model rather than the usual(1) three-band Hubbard model of cuprates. The model reads $H = H_1 + H_2$ with,

$$H_1 = \sum_{i,\sigma} e_i c^\dagger_{i\sigma} c_{i\sigma} + \sum_{i\neq j,\sigma} t_{ij} c^\dagger_{i\sigma} c_{j\sigma}, \quad [S1]$$

$$H_2 = \sum_i U_i c^\dagger_{i\downarrow} c_{i\downarrow} c^\dagger_{i\uparrow} c_{i\uparrow} + \sum_{\langle i\neq j\rangle,\sigma,\sigma'} U_{ij} c^\dagger_{j\sigma'} c_{j\sigma'} c^\dagger_{i\sigma} c_{i\sigma} + \sum_{\langle i\neq j\rangle,\sigma,\sigma'} K_{ij} c^\dagger_{i\sigma} c_{i\sigma'} c^\dagger_{j\sigma'} c_{j\sigma}, \quad [S2]$$

where the operator $c^\dagger_{i\sigma}$ creates a *hole* of spin σ and the index i runs through the Ag $d_{x^2-y^2}$ and the F $p_{\parallel,z}$ orbitals defined in Fig. S2. e_i and t_{ij} are single particle and hopping matrix elements respectively. Holes repel each other with strength U_i on orbital i and strength U_{ij} between different orbitals i and j. K_{ij} is the direct exchange interaction between different orbitals (usually ferromagnetic, i.e. $K_{ij} < 0$).

Estimate of hopping matrix elements. We discuss the more relevant hopping matrix elements for the nearest-neighbor magnetic interaction. Other matrix elements and further details will be presented elsewhere. We define t_{pd} as the hopping matrix element of an hypothetical straight L-F-R bond ($\eta = 180^\circ$) keeping the Ag-F distances constant. In this case only the $p_\parallel$ orbital mixes significantly and the hopping matrix element is $t_{pd} \equiv (\sqrt{3}/2)(pd\sigma)$ where $(pd\sigma)$ is the usual Slater-Koster(3) parameter. We find that $(pd\pi)$ matrix elements do not play an important role therefore, as customary for cuprates, we neglect them in the present computation.

Referring to Fig. S2, matrix elements are defined by the following equations,

$$\begin{aligned} H_1|d_L\rangle &= -t_{\parallel d}|p_\parallel\rangle + t_{zd}|p_z\rangle, \\ H_1|d_R\rangle &= t_{\parallel d}|p_\parallel\rangle + t_{zd}|p_z\rangle, \end{aligned} \quad [S3]$$

where we introduced,

$$t_{\parallel d} \equiv t_{pd}\sin(\eta/2), \qquad t_{zd} \equiv t_{pd}\cos(\eta/2). \quad [S4]$$

We can obtain a first estimate of the straight-bond parameter t_{pd} from band structure computations in related compounds. Refs. 4, 5 report t_{pd} for hypothetical solids with various F-Ag distances. We have estimated t_{pd} in AgF_2 using the scaling of Ref. 6 to extrapolate to the equilibrium bond distances in AgF_2 (Fig. S4) and obtained $t_{pds} = 1.39$ eV and $t_{pdl} = 1.37$ eV where s/l refer to the nonequivalent short (2.067Å) and long (2.074Å) bonds present in the structure. Using Eq. (S4), we obtain the pd-hopping matrix elements labeled "Slater-Koster" in Table S1.

A more direct determination can be obtained by performing an unpolarized DFT computation of AgF_2 followed by a parametrization of the bands in terms of Wannier orbitals which can be done using the maximally-localized projection scheme as implemented in the Wannier90 code(7). Figure S3 shows in red the DFT band structure in the region of the pd-bands. The blue lines are the bands obtained with the Wannier90 code with one d-like Wannier orbital centered on each Ag and two p-like Wannier orbitals centered on each F (5-band model) adopting the same local reference frame as defined in Fig. S2. Parameters are optimized to represent as best as possible the bands that cross the Fermi level inside a "frozen" energy window (shown in Fig. S3). Indeed, we see that this goal is well fulfilled. Other bands are not expected to be reproduced since they are dominated by orbitals not in the five-band model. In particular, as can be seen from the left panel, the bands immediately below the froze window and above -3 eV have dominant $p_\perp$ character and d character different from $x^2 - y^2$. Below that region significant weight in the orbitals of the five-band model appears again. This region, being far from the Fermi level is not constrained to be reproduced in detail but general features, as the overall bandwidth, is well reproduced by the Wannier parametrization, which is enough for our propose.

We checked that the optimized orbitals obtained with Wannier90 correspond closely to the $d_{x^2-y^2}$ and the $p_{z,\parallel}$ orbitals defined above which confirms this simple picture. Furthermore, the values of the hopping parameters (Table S1) corresponds fairly well (except for t_{dzl}) with the values estimated using a single Slater-Koster parameter and structural information. If

we perform the Wannier90 optimization with *all d*- and *p*-orbitals, one obtains a fit of the DFT band structure in the -7 eV to 1 eV energy window indistinguishable from the DFT bands. The resulting hoppings (last row in Table S1) match almost perfectly the values obtained with the Salter-Koster parametrization. This indicates that the slightly different parameters of the five orbital Wannier computation, take into account indirect hopping processes though the neglected orbitals and therefore such values are the recommended ones in a five-band model.

As with the analysis of Fig. S4 the parameter t_{pd} obtained from Wannier90 is very close to the value accepted for cuprates(8) ($t_{pd} \sim 1.3 - 1.6$ eV) although, as will be discussed below, because of buckling the resulting magnetic interaction is smaller. Regarding in plane fluorine-fluorine hoppings we find that they are on the range $t_{pp} \sim 0.13 - 0.3$ eV which is roughly a factor of two smaller than accepted values for oxygen-oxygen hoppings in cuprates ($t_{pp} \sim 0.65$). This is expected as distances are generally larger than in cuprates and the F's orbitals are more localized than those of O's. Another important difference is that for AgF_2 small but non-negligible fluorine-fluorine hoppings connect different planes in specific directions. This will result in longer-range magnetic interaction as will be clear from the polarized DFT computations.

Estimate of the on-site repulsion and the charge transfer energy. Here we provide details of the estimate of the strength of the Coulomb interaction on the Ag $4d$ orbitals using the empirical information available and polarized DFT computations.

As mention in the main text, in solids the Hubbard interaction $U = U^0 - R$ is strongly screened respect to the free ion value, U^0, due to the relaxation of the environment. As it is well known R can be quite large, for example for the d shell of Cu, $U_d^0 = 18.6$ eV for free ions and gets reduced to $9 \sim 10$ eV in oxides(9–12). A rough estimate of R can be obtained assuming that the relaxation is dominated by the polarization of the neighbors (9, 12) due to the electric field $\pm e/d_i^2$ of added/removed electrons. Here d_i is the distance to the neighbor. This yields,

$$R = 2\sum_i P_i, \qquad [S5]$$

with $P_i = \alpha e^2/(2d_i^4)$. The sum runs over neighbors assumed to have polarizability α. For oxygen(13) α varies in the range $\alpha_O = 0.5 \sim 3.2$ Å^3. In the case of La_2CuO_4, $\alpha_O \sim 1.9$ Å^3 is needed to obtain $R \sim 10$ eV.

Unfortunately, direct probes of U_d in AgF_2 are not available. As mentioned in the main text, estimates of solid state values can be obtained by examining experiments on closed d shell systems where Auger spectroscopy gives a direct measurement of U_d according to Cini-Sawatzky theory(14, 15). First estimates of U_d were obtained by Powell analyzing the Auger spectra of the noble metals. We can check the relevance of this measurements for our propose comparing the case of pure Cu metal and Cu in oxides. For elementary Cu, Powell concluded that $U_d = 7.7$ eV, similar to the value obtained by Sawatzky and collaborators(16) and somehow below to the value accepted in parent high-T_c cuprates, $U_d \sim 8 \sim 10$ eV(8, 10). The strongest screening in the metal respect to the oxide can be attributed to screening by the open $4s$ shell. Since Ag atom is larger than Cu atom, for elementary noble metals we expect larger polarizability and a smaller bare Coulomb integral in the former respect to the latter. Consistently $U_d = 5.1$eV is found in elementary Ag(17, 18), smaller than Cu but still quite large. Again, this value should be taken as a lower bound for U_d in AgF_2 because of the additional screening of $5s$ electrons.

A more realistic value of U_d for its use in AgF_2 can be obtained from the analysis of Auger spectra in Ag_2O where Ag is in the d^{10} configuration. For comparison in the case of Cu_2O (also d^{10}) $U_d = 9.2$ eV was obtained by Tjeng, Sawatzky and collaborators(11). This is close to standard value used in superconducting cuprates although in the latter case screening is expected to be larger due to the larger number of nearest neighbor O's. In the case of Ag_2O, they obtained $U_d = 5.8$ eV which could be explained with a screening $R = 9$ eV. This is underestimated with Eq. (S5) and $\alpha_O = 3.2$ Å^3 which yields $R = 5.2$eV.

Polarizabilities have units of volume and tend to scale with ionic volumes. Indeed, F^- has a smaller polarizability(13) due to the more compact orbitals, $\alpha_F = 0.64$ Å^3, and the d_i distances are smaller so Eq. (S5) yields $R \sim 2.4$ eV for the screening of U_d in AgF_2. If taken literally this would imply $U_d = 12.4$ eV, but given the above underestimation of the screening in Ag_2O we suspect that this value of U_d is too large. In any case, we see that the expectation of smaller values of U_d in the $4d$ shell respect to the $3d$ shell can be compensated by poorer screening. These estimates, however, are too crude to obtain practical values of U_d in the solid and are presented only to show that expectations based solely on the extension of the orbitals may be too crude too. The physical value should be smaller than the Eq. (S5) estimate but larger than the one found in the metal i.e. 5.1 eV$< U_d <$ 12.4 eV. This indicates that a value similar to the one in cuprates is quite reasonable.

An alternative estimate can be obtained from the distance between Hubbard bands in hybrid DFT and indicated with red arrows in Fig. 2. This yields $U_d = 10.7$ eV (La_2CuO_4) and $U_d = 9.4$ eV (AgF_2). For concreteness in the computations of magnetic interactions below we use the latter value. Clearly more accurate theoretical and experimental determinations are called for.

Another important parameter is the charge transfer energy Δ which can be defined as the energy cost to transfer a hole from the d shell of the transition metal to the p shell of the ligand in the absence of hybridization, ($d^9 + p^6 \rightarrow d^{10} + p^5$). We notice that the insulating gap in the hybrid DFT computation for La_2CuO_4 (Fig. 2) is very close to the value of the charge transfer parameter ($\Delta \equiv e_d - e_p$) estimated from constrained DFT(8) computations $\Delta = 3.5$ eV. Thus, we use the gap in the AgF_2 computation as a proxy to estimate $\Delta = 2.7$ eV. For simplicity we neglect the crystal field splitting between the p orbitals.

Finally, given the more compact p orbitals in fluorine the bare Coulomb interaction should be larger than for oxygen but we expect this to be partially compensated by a larger screening due to a polarizability of silver larger than copper so we take $U_p = 4$ eV, close to typical values in cuprates.

Magnetic interactions. Our aim here is to describe the magnetic excitations of the system with a Heisenberg model,

$$H = \frac{1}{2}\sum_{ij} J_{ij}\mathbf{S}_i.\mathbf{S}_j, \qquad \text{[S6]}$$

where the sums run over all Ag sites and $\mathbf{S}_i$ is a spin 1/2 operator. The similarity of the parameters estimated above for AgF_2 with the ones for cuprates suggest that the nearest-neighbor antiferromagentic interaction J, should be large in the present compound. We first use perturbation theory to estimate the order of magnitude and discuss the effect of buckling for the nearest-neighbor exchange interaction. Then we present a DFT computation to examine longer range interactions, estimate the degree of anisotropy and estimate the Néel temperature.

Perturbative computation. We consider again the L-F-R of Fig. S2. The antiferromagnetic interaction among nearest-neighbor spin-1/2 Ag sites is the result of two opposite mechanisms: Anderson's superexchange(19) and direct exchange. An important point is that due to buckling the p_z orbital of Fig. S2 cannot be neglected.

A first estimate of the nearest-neighbor interaction can be done using perturbation theory. Direct exchange appears at second order in the hopping while superexchange appears at fourth order. One obtains, $J = J^{(2)} + J^{(4)}$, with,

$$J^{(2)} = 2t_{\parallel d}^2\left(\frac{1}{\Delta - K_{\parallel d}} - \frac{1}{\Delta + K_{\parallel d}}\right), \qquad \text{[S7]}$$

$$J^{(4)} = \frac{\left(t_{\parallel d}^2 - t_{zd}^2\right)^2}{\Delta^2}\left(\frac{4}{U_d} + \frac{8}{2\Delta + U_p}\right) = \cos^2(\eta)\frac{t_{pd}^4}{\Delta^2}\left(\frac{4}{U_d} + \frac{8}{2\Delta + U_p}\right). \qquad \text{[S8]}$$

Here, given the uncertainties in parameters, we made various simplifying assumptions. We neglected the small difference in hopping matrix elements due to short and long Ag-F bonds reported in Table S1. Similarly to the case(20) of $CuGeO_3$, both the Hund's rule exchange among the p orbitals and the direct exchange between p and d orbitals yield a ferromagnetic contribution. However, the former appears at fourth order in the hopping so it was neglected. Only the dominant direct exchange parameter with the $p_\parallel$ orbital, $K_{\parallel d}$, was retained. Another simplification was to take a single parameter U_p for the repulsion of two holes on the same p orbital or on different p orbitals. Also for simplicity, we neglected the nearest neighbor repulsion U_{pd} which can be partially absorbed in the definition of Δ.

Because the p_z orbital is even respect to an exchange of L and R while the $p_\parallel$ is odd, tunneling process though these orbitals interfere destructively as it is clear from the prefactor in Eq. (S8). Clearly, such effect tends to reduce the superexchange interaction $J^{(4)}$, respect to a flat configuration ($t_{zd} = 0$).

As a reference, and according to the previous estimates we can take, $t_{\parallel d} = 1.24$ eV, $t_{zd} = 0.65$ eV, $U_d = 9.4$ eV, $U_p = 4$ eV, $\Delta = 2.7$ eV. With these parameters and neglecting direct exchange one obtains $J = J^{(4)} = 0.22$ eV. Such value is too large to be taken seriously but shows that even in the presence of buckling large values of the magnetic interaction are possible. Such overestimation is also common to cuprates when the direct exchange is neglected(8, 20**?** , 21). Experimentally $J = 0.07$eV is obtained in the main text. This requires $K_{\parallel d} = -0.17$ eV, which is of the order of typical values in cuprates(8, 20**?** , 21).

The above discussion clarifies the role of buckling on the determination of the magnetic interaction. In addition the similarity of microscopic parameters of AgF_2 with the ones of cuprates have been emphasized and we showed that a large value of J is not incompatible with the present knowledge of parameters. In the following we present a computation of magnetic interactions based on DFT which confirms this concussion.

Density Functional Theory computations and Néel Temperature. To compute magnetic interactions with DFT one can use either a total energy method(22) (TE) or the magnetic total force theorem (MTFT)(23). The latter has the advantage that interactions of arbitrary range can be computed within one computation. We use the latter as implemented in Ref. 24 for a general exploration of interactions and perform total energy computations to check the results in specific cases.

For the magnetic total force theorem computations, the Green's functions and the local spin-dependent Hamiltonian matrix elements were evaluated using a set of maximally localized Wannier functions calculated with the Wannier90 software interfaced with VASP. This set is different from the Wannier computation of the previous section because only one Wannier orbital per Ag site is retained.

Table S2 shows the exchange interactions computed by the two methods. The theoretical nearest neighbor interaction results to be around 1/2 of typical values in cuprates. Despite the fact that some bands in the paramagnetic electronic structure have non-negligible dispersion in some of the out of plane directions (Fig. S3) the magnetic interactions are quite anisotropic.

In order to estimate the Néel temperature we have performed classical Monte Carlo simulations of model Eq. (S6) with spins substituted by classical vectors of length 1/2 and parameters from the MTFT computations of Table S2. Such simulation yields $T_N^{class} = 90$ K. However, treating the spin as classical is a very rough approximation for a spin-1/2 system. To investigate this effect we performed classical simulations of a simple three-dimensional Heisenberg model on a square lattice for which fully quantum mechanical simulations are available(25). Comparing the classical and the quantum simulations for systems of similar ratio of the interlayer to intralayer coupling α we arrive at the conclusion that the quantum $T_N = \gamma(\alpha)T_N^{class}$ with $\gamma = 2.3$ for the anisotropy of AgF_2 (γ depends weakly on α so a precise determination is not necessary). This yields $T_N = 207$ K for the theoretical Néel temperature of AgF_2 to be compared with the experimental value $T_N = 163$ K. Since, as explained in the main text, we find experimentally that the nearest neighbor magnetic coupling is even larger than the one of the MTFT method we

attribute the difference to longer-range coupling. Indeed, we find that such couplings are very sensitive to details of the method while the nearest neighbor coupling is much more robust. For example, using non-optimized Wannier orbitals we find that long-range coupling can change by a factor of 2 while the nearest neighbor coupling changes by 10%. Another source of error may be additional terms in the Hamiltonian not considered here like four-site cyclic exchange(26) and Dzyaloshinsky-Moriya interaction. Given these approximation we find that the theoretical Néel temperature of the same order as the experimental one confirms the presence of robust magnetic interactions in AgF_2 as in cuprates.

Methods

Sample preparation. Powder samples were prepared in-house starting from $AgNO_3$, anhydrous HF treated with K_2NiF_6, and elementary fluorine. In typical synthesis, 3 g of silver(I) nitrate ($AgNO_3$) was weighted into the FEP (tetrafluoroethylene-hexafluoropropylene block copolymer) reaction vessel (16 mm i.d., 19 mm. o.d., length = 18 cm; equipped with PTFE valve) in a dry-box. Anhydrous HF (20 ml, Linde, 99.995%), treated with K_2NiF_6 (Advance Research Chemicals, Inc.) for several hours prior to use, was condensed onto $AgNO_3$ at 77 K. The reaction vessel was brought to ambient temperature and a clear colourless solution was obtained. Elemental fluorine was slowly added at ambient temperature till the pressure in reaction vessel reached 4 bar. Precipitation of a brown solid was observed. The stirring of the reaction mixture at ambient temperature was carried out. After one day, the reaction vessel was cooled down to 77 K, volatiles pumped away, reaction mixture brought to ambient temperature and the new portion of fluorine was added. The whole procedure has been repeated several times. With the last portion of fluorine, which was already in an excess the reaction mixture was left for 2–3 days. After that the liquid phase was decanted away and the volatiles were pumped away overnight at ambient temperature. The freshly prepared sample was used for research as described below. A commercial reference sample of AgF_2 was obtained from Sigma Aldrich. Samples where enclosed in sealed quartz capillaries for further manipulation and characterization.

Sample characterization by powder X-ray diffraction. Powder X -ray diffraction pattern (XRDP) with $CoK\alpha$ radiation was recorded at room temperature for freshly prepared and purchased AgF_2 samples enclosed in a 0.3 mm quartz capillary. The XRDPs are shown in Fig. S5 and indicate the presence of a small amount of AgF impurity in both samples (reflections from AgF are somewhat larger in commercial AgF_2 than in a freshly prepared sample) as well as three reflections from unknown impurities (seen only for commercial AgF_2; they do *not* originate from $AgNO_3$, which is a common precursor of AgF_2).

Sample characterization by heat capacity measurements. Heat capacity measurements were conducted for milligram quantities of AgF_2. In order to prevent reaction with moisture each sample was wrapped in aluminum foil in a glovebox and then transferred to the Physical Property Measurement System (MPMS, Quantum Design) for measurements. The obtained heat capacities were corrected for the signal from aluminum(27).

The heat capacity of AgF_2 (Fig. S6) show a λ type anomaly due to magnetic ordering at 161 K. The entropy change at the phase transition (estimated by integrating $c_p\,/\,T$ at λ peak in the 145–165 T range) equals 0.28 J mol^{-1} K^{-1}, i.e. only 5 % of Rln(2) value expected for full ordering of spin 1/2 system. Thus, the high-T paramagnetic phase must exhibit substantial short-range antiferromangetic interactions (as for(28) $CuCl_2$). Partial ordering above the Néel point suggest in turn the presence of appreciable magnetic superexchange between the Ag^{2+} centers.

Sample characterization by High-Field Electron Paramagnetic Resonance. High-field, high-frequency electron paramagnetic resonance (EPR) spectra at temperatures ranging from ca. 3 K to 290 K were recorded on a home-built spectrometer at the EMR facility of the NHMFL(29). The instrument is equipped with a superconducting magnet (Oxford Instruments) capable of reaching a field of 17 T. Microwave frequencies over the range 52-416 GHz were generated by a phase-locked Virginia Diodes source, producing a base frequency of 13 ± 1 GHz, which was multiplied by a cascade of frequency multipliers. The instrument is a transmission-type device and uses no resonance cavity. A liquid He-cooled InSb bolometer (QMC Instruments Ltd) was used as a microwave detector. All spectra were taken in derivative mode, $\mathrm{d}I\,/\mathrm{d}B$ (where I is the absorption intensity), using field modulation and a phase-sensitive lock-in detection scheme. Since the samples are moisture-sensitive, they were packed in air-tight sample holders ($\varnothing_{\mathrm{in}}$= 7 mm, $\varnothing_{\mathrm{out}}$= 9 mm, l = 26 mm) made from perfluoropolymers, and protected with two tightly fitting PTFE (Teflon®) stoppers (l = 28 mm).

We searched for EPR signal using fields from 0 to 14.9 T and frequencies ca. 50-640 GHz at temperatures ranging from ca. 3 K to 200 K and found no signal which could be attributed to the bulk of the sample, a situation that mirrors cuprates(30).

Sample characterization by far infrared absorption spectroscopy. The far infrared (FIR) spectrum has been collected in the transmission mode in a Vertex 80v spectrometer (from Bruker) equipped with a globar light source. A mylar beam splitter and DTGS detector were used. The measurement set-up included two PTFE optical windows spaced by a 0.1 mm thin separator; the fine AgF_2 powder was dispersed on the internal side of one of the windows.

Comparison of phonon frequencies with DFT calculations and mode assignment. We compared the experimental Raman and far infrared (FIR) phonons with the theoretical predictions based on the DFT computations. The purpose is twofold. On one hand, good agreement between theory and experiment allows to validate the accuracy of the DFT computations. On the other hand, AgF_2 can easily decompose due to excessive illumination or reaction with containers or even traces of moisture thus vibration spectroscopy allows to check the integrity of the sample. Including the IR phonons in the analysis ensured that the full phonon assignment is robust. In the following we present both the IR and Raman vibrational analysis.

The unit cell has 4 formula units which yields 36 Γ-point frequencies. Symmetry analysis yields the following irreducible representations:

$$AgF_2 : 3A_g + 6A_u + 3B_{1g} + 6B_{1u} + 3B_{2g} + 6B_{2u} + 3B_{3g} + 6B_{3u}$$

The acoustic modes transform like B_{3u}, B_{2u} and B_{1u}. Of the remaining modes 15 should be IR active (8 of those are observed), 12 should be Raman active (11 of those are observed), and 6 should be silent.

For the classification of the modes here and in Table S3 we adopt a coordination system different from the main paper and such that $[AgF_2]$ sheets are in the *ac* plane, while *b* axis is perpendicular to them.

Hybrid functional DFT is considered to perform better than DFT+U and was used to obtain more accurate vibrations frequencies but the intensity computation was restricted to the DFT+U method for technical reasons. The theoretical wavenumbers coming from DFT+U calculations or hybrid functional DFT are presented in Table S3 as-obtained, i.e. without any scaling to fit the data.

The DFT+U calculations tend to reproduce the IR spectrum reasonably well (Fig. S7**b**). The largest intensity is computed for the 441 cm^{-1} band (B_{3u}), which is indeed the strongest band in the experimental spectrum (also, its wavenumber is identical to the theoretical value). This band is assigned to B_{3u} Ag-F stretching mode, which corresponds to local deformation of the local $[AgF_4]$ square towards the (2+2) bent cis-$[F_2...AgF_2]$ unit.

Substantial intensities are also computed for the 453 cm^{-1} band (it is too close to the main feature to be distinguished from it clearly) as well as for the 310 and the 312 cm^{-1} bands (there is a feature at 307 cm^{-1} in the experimental spectrum), for the 185 cm^{-1} band (exp. 193 cm^{-1}), for the 134 cm^{-1} band (there is a shoulder at ca. 139 cm^{-1} in experimental spectrum) and for the 90 cm^{-1} band (the experimentally seen band at 93 cm^{-1} is stronger than predicted). The bands seen in experiment at 159 and 168 cm^{-1} have their intensities underestimated by theory (for bands at 156 and 163 cm^{-1}, respectively). Despite these discrepancies, the bands appearing in the experimental spectrum may be rather easily assigned.

Since absolute wavenumbers of the IR-active modes were predicted with the accuracy better than 10 cm^{-1}, one may base the assignment of Raman-active modes on the assumption that their calculated wavenumbers are fairly correct, too, while the intensities may differ from the experimental ones. This assumption is not unreasonable since Raman intensities are inherently difficult to predict.

The Raman spectra in the phonon region for various excitation energies is shown in Figure S7**a**. The spectra taken with the three laser lines are quite similar. The spectrum taken with 1064 nm (1.17 eV) excitation is predominated by a strong band at 254 cm^{-1}, which is assigned to the B_{2g} mode (for assignment of this and other bands see Table S3). Several weaker features appear, particularly at 168, 183, 198, 314, and 486 cm^{-1}. The broad band at *ca.* 970 cm^{-1} is also seen.

For the excitation with 514.5 nm (2.41 eV) a mode at 417 cm^{-1} relatively gains on intensity. Since the intensity of this mode grows with the photon dose we assign it to an impurity phase generated via a photochemical processes.The absence of this band was monitored to check the integrity of the sample for both vibrational and electronic Raman measurements.

Importantly, the strongest calculated Raman band at 253 cm^{-1} is found at 254-258 cm^{-1} in the experimental spectra. This band is assigned to the B_{2g} mode involving the Ag-F stretching, which leads to the formation of quasi-1D kinked-chain structure $(AgF^+)(F^-)$. The relative intensities of four Raman-active bands in its vicinity are not predicted very accurately, as expected, but their wavenumbers agree very well with the experimental values (311 exp. *vs.* 309 cm^{-1} theor.; 290 exp. *vs.* 296 cm^{-1} theor.; 244 exp. *vs.* 249 cm^{-1} theor.; 232 exp. *vs.* 227 cm^{-1} theor.). The last important band which is predicted to be quite intense in Raman spectrum is the one positioned at 443 cm^{-1} (B_{2g}). We find a weak Raman feature at 446 cm^{-1} in some of our spectra, which we tentatively assign to this B_{2g} mode.

Having assigned fundamentals, it is now possible to understand the origin of the broad structured band appearing at 970 cm^{-1} in spectra measured with 1064 nm or 514.5 nm excitation (see main paper). This band likely originates from the first overtones of the highest-frequency Raman (B_{3g} 478 cm^{-1}, B_{2g} 481 cm^{-1}), IR-active (B_{1u} 470 cm^{-1}, B_{2u} 468 cm^{-1}) and silent modes (A_u 477 cm^{-1}). The first overtones for all of them are totally symmetric (A_g) and likely resonance-enhanced, particularly at 514.5nm excitation . Since two phonons are combined the total momentum of the pair is restricted to be zero but one of the constituents can have arbitrary momentum which explains the broad structure.

Respect to the group theory analysis, 1 extra band appears in the IR spectrum (shoulder at 497 cm^{-1}), and 4 extra bands in Raman spectra (138 cm^{-1}, 368-377, 413-419, and 480-485 cm^{-1}). In Table S3 we propose their assignment to the corresponding overtones and/or combination modes, using match of wavenumbers and symmetry considerations.

Based on the analyses presented above, supplemented by more thorough analysis of all weak features, we obtain the band assignment shown in Table S3.

Simulation of the Inelastic Neutron Scattering spectra. In order to simulate the inelastic neutron scattering spectra of our powder samples we used the SpinW software (31). How the overall intensity changes as one moves from one Brillouin zone to the next depends on the magnetic form factor. Since the atomic form factor of Ag^{2+} is not available we used the Pd^+ form factor which is also a $3d^9$ ion. The results are shown in Fig. S8**a** for an incident energy $E_i = 300$meV to be compared with Fig. 4 of the main text. We see that the plume emanating from the ordering wave-vector is well reproduced (indicated) but the intensity of the flat band is peaked at much smaller wave vectors respect to the experiment. Indeed, the atomic form factor decays quite fast with momentum as seen in Fig. S8**c**.

Similarly to Ref. (32) we computed DFT form factors for AgF_2 by first obtaining Wannier orbitals on top of the hybrid-DFT computations with five *d*-orbitals per Ag ion and three *p*-orbitals for F ion. Then the $d_{x^2-y^2}$ orbital corresponding to the

fluctuating spin is used to compute the form factor. Cuts of the resulting anisotropic form factor are shown in Fig. S8**b**. We see that the in the c-axis direction (z) the form factor is very similar to the atomic form factor of Pd^{+} consistent with the fact that the hybridization of orbitals in the c-direction is small. For the in-plane directions (x and y) the form factor has a strong oscillation and a negative minimum at a finite wave-vector. This originates in the $d_{x^2-y^2}$ orbitals which is strongly hybridized with the surrounding F p orbitals pointing in the bond direction. Thus, the fluctuating magnetic moment has an oscillating tail in real space which produce a finite momentum minimum when Fourier transformed. Notice that the strength of the form factor at high momentum can be comparable to that of the atomic Cu^{2+} ion. Ultimately, the large intensity observed for the flat band at large momentum in the experiment (Fig. 4) is consistent with a strongly covalent Ag-F bond as suggested also by the DFT computations.

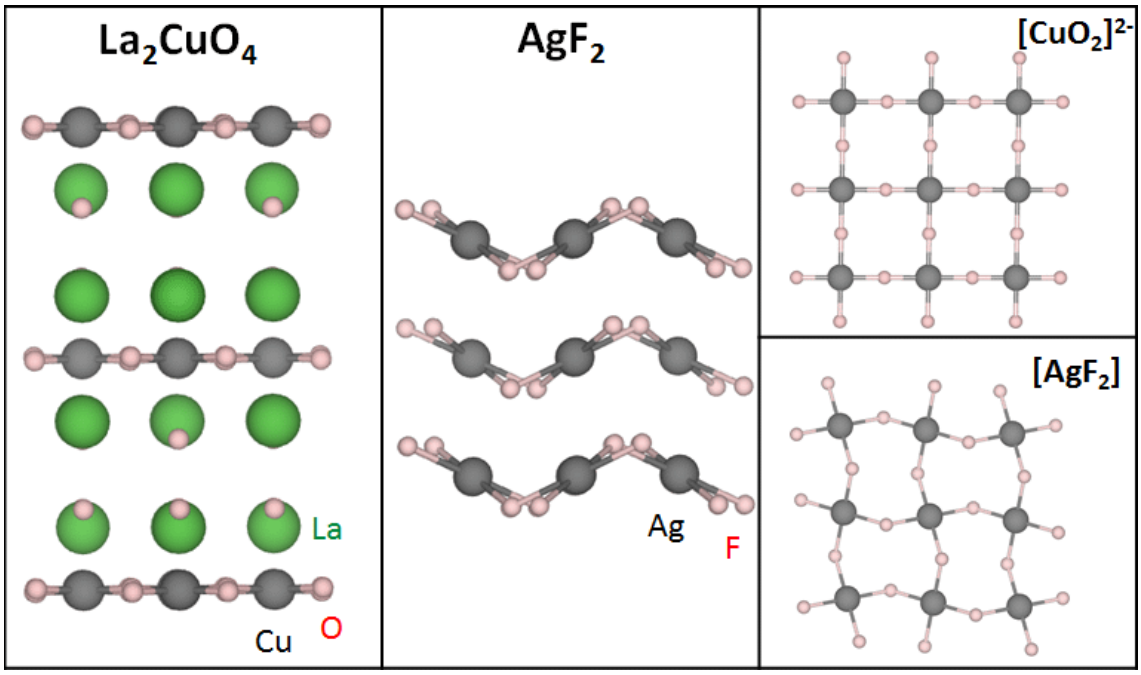

Fig. S1. **Comparison of the crystal structure of La_2CuO_4 and AgF_2.** Notice that for the cuprate layers formed of charged $[CuO_4]^{-6}$ units are compensated by the $[La_2]^{+6}$ spacer layers. Instead, the $[AgF_2]$ layers are intrinsically neutral and charged spacing layers are not required. Notice the similarity of the sheet topology shown on the right panels.

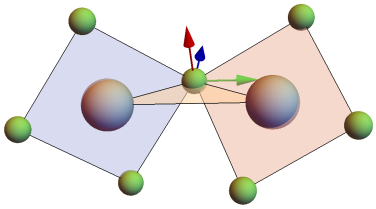

Fig. S2. **Schematic representation of an Ag-F-Ag bond** Gray (green) spheres represent Ag (F) atoms. $d_{x^2-y^2}$ orbitals are label as d_L and d_R for the left and right Ag respectively. They are defined in such a way that the lobs are oriented approximately along the diagonals of the approximate squares defined by F's (light blue and salmon). We also show the triangle defined by the central F and the two Ag's. The arrows represent the direction taken for the p orbitals ($p_\perp, p_\parallel, p_z$). Red is orthogonal to the triangle plane and defines the $p_\perp$ orbital. Green ($p_\parallel$) is parallel to the Ag-Ag bond while blue (p_z) is contained in the triangle plane, is perpendicular to the Ag-Ag bond and points approximately in the c direction.

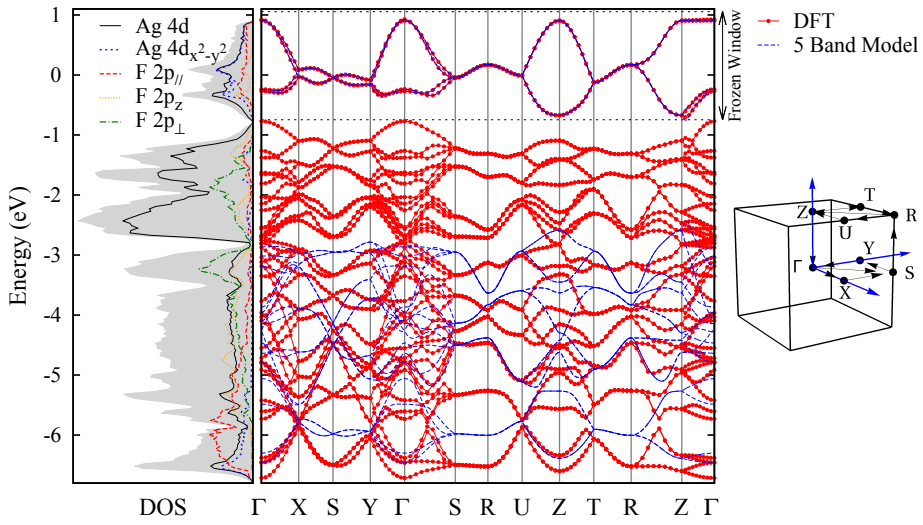

Fig. S3. $\mathbf{Unpolarized\ band\ structure\ of\ AgF_2}$**.** The right panel show the DFT bands obtained with VASP in the region dominated by F-$2p$ and Ag-$4d$ orbitals (red) and the bands obtained with the Wannier90 code (blue) using a Wannier basis with one d and four p orbitals per formula unit (5-band model). Wannier orbitals are optimized to match the bands within the indicated frozen window. This provides accurate bands around the the Fermi energy which is located at zero energy. The inset shows schematically the path around the Brillouin zone. The filled gray curve in the left panel is the total density of states (DOS) while the other curves are the orbital resolved DOS.

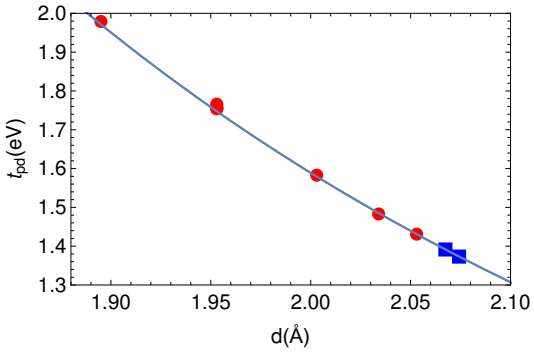

Fig. S4. Hopping matrix elements vs. F-Ag distance (d) Red dots are from Refs. 4, 5. Extrapolation was done assuming Andersen scaling(6), $(pd\sigma) = (pd\sigma)^0(d_0/d)^4$ (blue line). The blue dots are the t_{pd} values estimated for the two possible Ag-F distances in AgF_2.

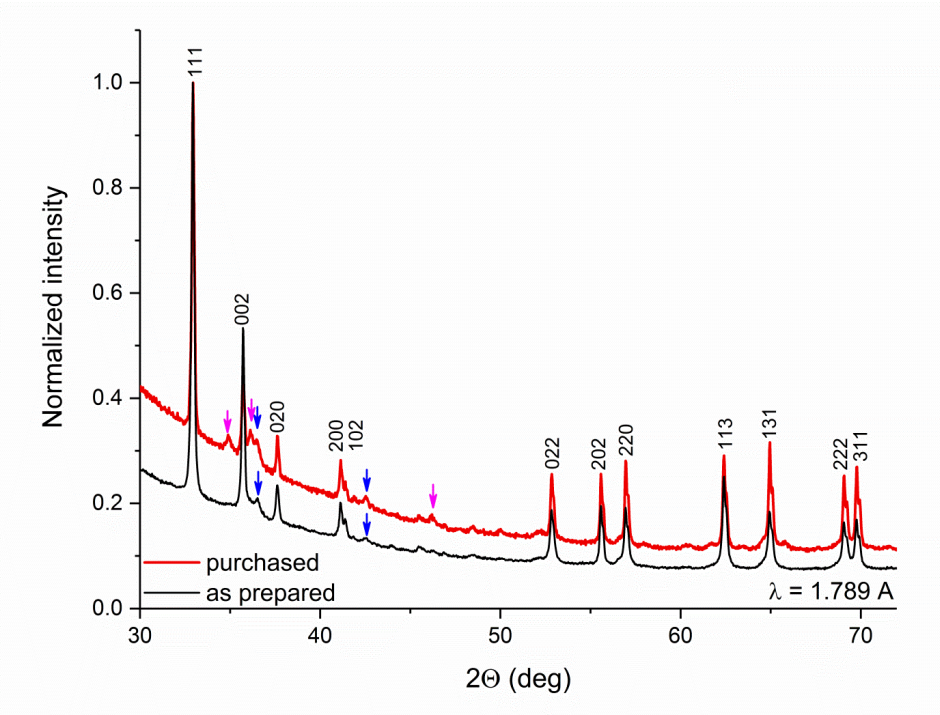

Fig. S5. X-ray characterization. Comparison of X-ray diffraction patterns ($\lambda(K\alpha_1)$ = 1.7890 Å, Co) for as-synthesized (black line) and commercial (red line) AgF_2. Blue arrows mark reflections coming from AgF, pink – from unknown impurities. The hkl indices from AgF_2 are given.

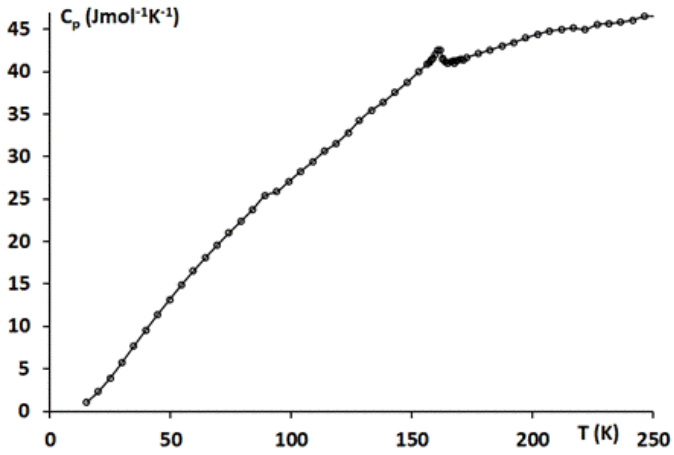

Fig. S6. $\mathbf{Heat\ capacity\ of\ AgF_2\ as\ a\ function\ of\ temperature.}$ The λ peak with the maximum at 161 K has been used for the estimate of magnetic entropy change at the phase transition.

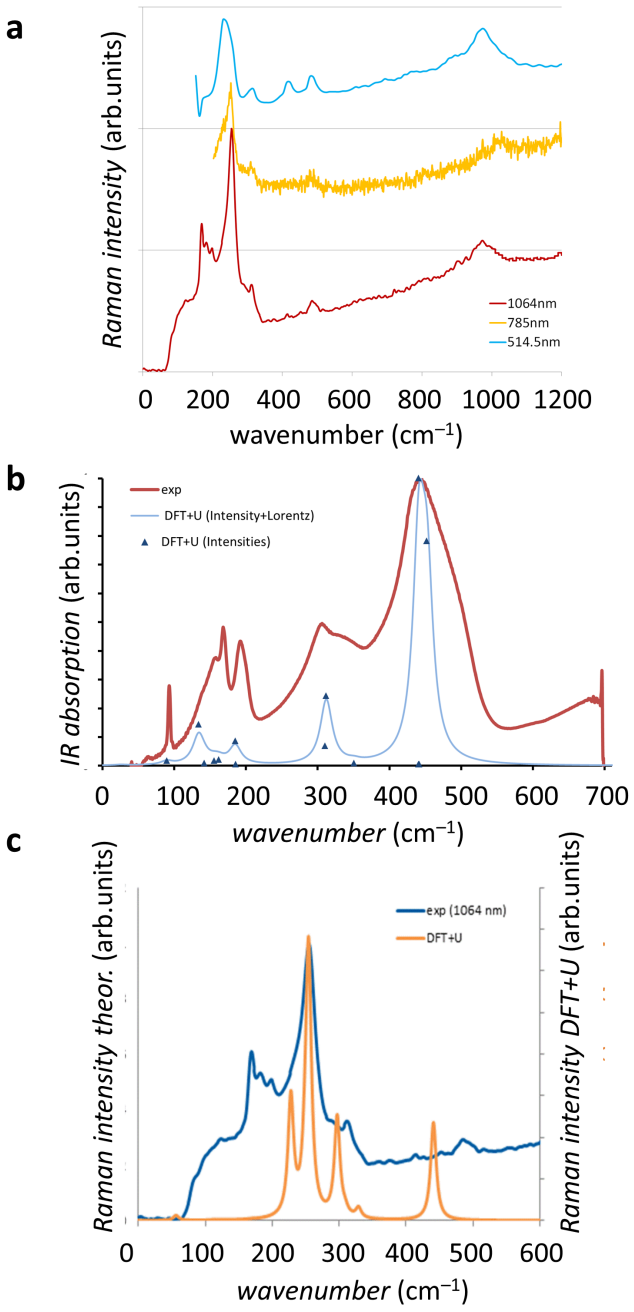

Fig. S7. Vibrational spectroscopy. **a** The Raman spectra of AgF_2 measured at different excitation lines. We show the range of fundamental modes (up to ca. 490 cm^{-1}) and overtones (up to ca. 970 cm^{-1}). **b** Comparison of the measured (red line) and simulated using Lorentzian functions (blue line) IR absorption spectrum of AgF_2 (dark blue triangles mark the positions and intensities of of IR-active modes calculated at DFT+U level, which were used for generating the simulated spectrum. **c** Comparison of the measured (blue line) and simulated (orange line) Raman spectrum of AgF_2.

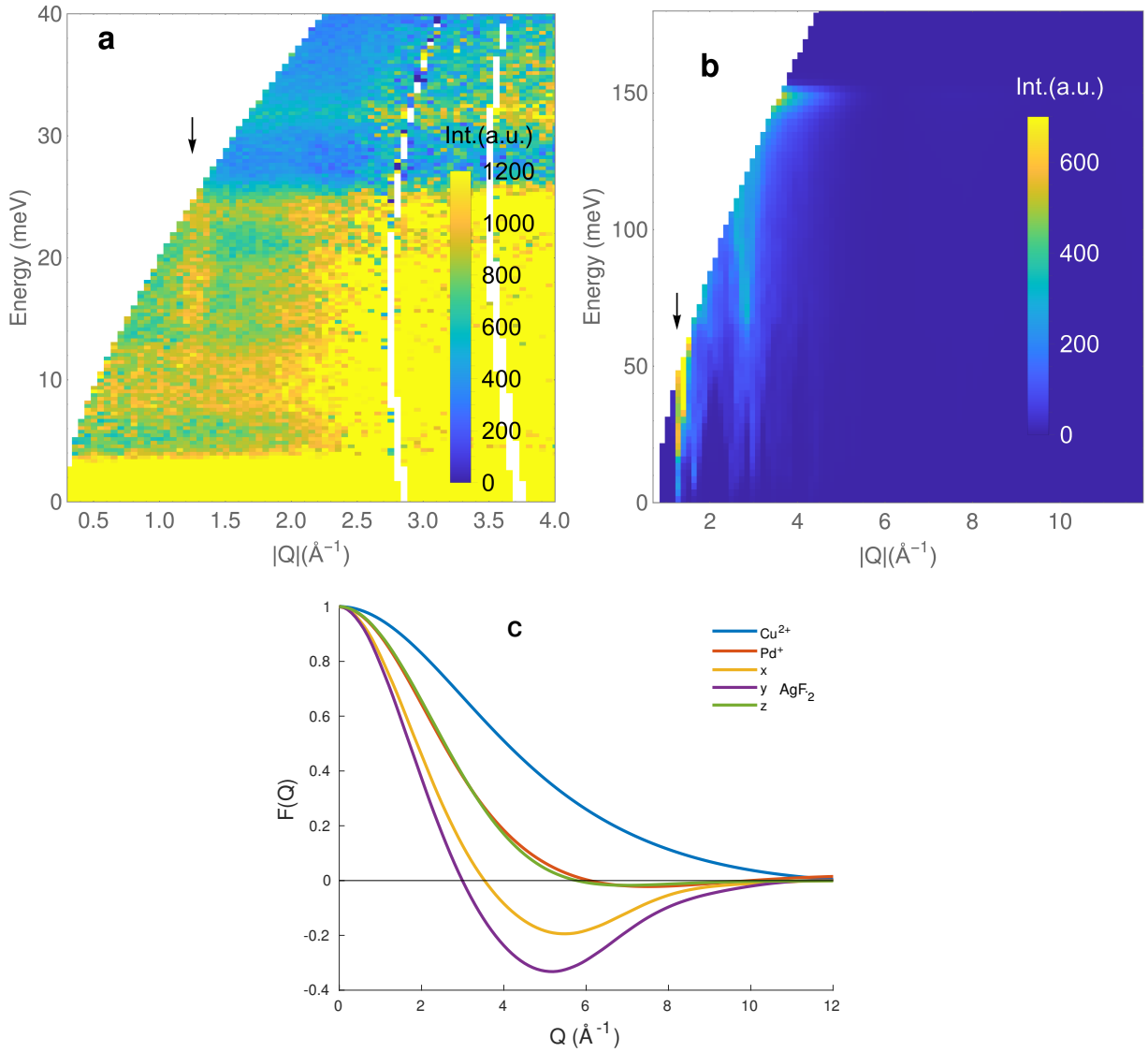

Fig. S8. Inelastic neutron scattering. Panel **a** shows an experimental scan with incident neutron energy $E_i = 60meV$. The arrow indicates the plume emanating from the ordering wave-vector and corresponding to the plume seen in the high energy scan of Fig. 4. Panel **b** shows the SpinW program(31) simulated powder averaged spectrum for $E_i = 300meV$ and the Pd^{+} atomic form factor from Ref. (33) to be compare with the computation used the hybrid-DFT form factor and shown in the main text. The spectrum was convoluted with the experimental resolution. Panel **c** shows the form factors used in the computations. The red curve is the atomic form factor of Pd^{+} ion from Ref. (33) that was used for the simulation in panel **b**. x, y, z labels cuts of the anisotropic AgF_2 form factor along the a, b, c crystallographic directions respectively. The form factor was obtained from hybrid-DFT computations as explained above. We also show the Cu^{2+} atomic form factor(33) for comparison (magenta line).

	$t_{\parallel dl}$	$t_{\parallel ds}$	t_{zdl}	t_{zds}
Slater-Koster	1.24	1.26	0.58	0.59
1+4 orbitals	1.20	1.28	0.73	0.58
5+6 orbitals	1.25	1.26	0.56	0.60

Table S1. Nearest neighbor pd hopping integrals (eV). Slater-Koster are the results extrapolated from the DFT computations of Ref. 4, 5 and Eq. (S4). The next two lines show the present Wannier90 computations with 5 and 11 orbitals per f.u. The subindex s/l refers to the non-equivalent short and long bonds present in the structure.

Mult.	Position diff.			J_{ij} (MTFT)	J_{ij}(TE)
	a	**b**	**c**	meV	meV
4	± 0.5	± 0.5	0	52	56
2	0	± 1	0	4.5	-
2	± 1	0	0	4.2	-
2	$\pm(1$	$-1)$	0	1.2	-
2	$\pm(1$	$1)$	0	1.1	-
4	$\pm(0.5$	$-1)$	± 0.5	0.45	-
2	0	$\pm(1$	$-1)$	-0.26	-
4	$\pm(0.5$	$1)$	± 0.5	0.11	-
4	0	± 0.5	± 0.5	0.576	-1.62
4	± 0.5	0	± 0.5	-0.15	-1.01
4	$\pm(1$	$0.5)$	± 0.5	-0.16	-

Table S2. Magnetic exchange constant. We show the exchange constant J_{ij} computed combining DFT+U and the MTFT method(24) and (for specific directions) combining hybrid-DFT and the TE method(22). DFT+U combined with TE method yields very similar values. Columns 2-4 are the difference in the position of Ag ions i and j in lattice units. In plane exchange constants less than 1 meV were neglected. The first column are the number of bonds with the same exchange matrix element (fixing the initial atom). $\pm(1 \quad -1)$ is a shorthand for $1 \quad -1$ and $-1 \quad 1$.

No.	Exp.IR	Exp. Raman	DFT+U	HSE06	Symm. (activity)	Comment
1	497sh					441+56 combination (B_{3u}) and/or 470 IR B_{2u} (HSE06)
2		480-485				254+233 combination (B_{2g}) and/or 481 Raman B_{2g} (HSE06)
3			461	477	A_u (silent)	
4			455	470	B_{2u} (IR)	
5			453	468	B_{1u} (IR)	
6		446	443	481	B_{2g} (Raman)	
7	441vs		441	459	B_{3u} (IR)	
8			441	478	B_{3g} (Raman)	
9		413-419				341+73 combination (B_{3g}) & photochemical product*
10		368-377				193+168 combination (B_{1g}) and/or 193 first overtone (A_g)
11	341sh		350	356	B_{3u} (IR)	
12		337	329	340	B_{1g} (Raman)	
13			323	325	A_u (silent)	
14	307m		312	317	B_{2u} (IR)	
15	307m		310	317	B_{1u} (IR)	
16		311-312	309	323	A_g (Raman)	
17		290-291	296	307	B_{1g} (Raman)	
18		258	253	257	B_{2g} (Raman)	
19		244	249	250	B_{3g} (Raman)	
20		232-233	227	232	A_g (Raman)	
21	193m		186	199	B_{2u} (IR)	
22	193m		185	195	B_{1u} (IR)	
23			183	200	A_u (silent)	
24		162-174	171	183	B_{2g} (Raman)	
25	168m		163	175	B_{3u} (IR)	
26			162	170	A_u (silent)	
27	159w		156	161	B_{3u} (IR)	
28			143	146	B_{1u} (IR)	
29	139sh		134	136	B_{2u} (IR)	
30		138				73+73 first overtone (A_g)
31		125	132	140	B_{3g} (Raman)	
32		102-117	115	118	B_{1g} (Raman)	
33			98	101	A_u (silent)	
34	93w		94	93	B_{3u} (IR)	
35	93w		90	92	B_{1u} (IR)	
36			73	72	A_u (silent)	
37		57	59	65	A_g (Raman)	
38	—		27	38	B_{2u} (IR)	range not measured

Table S3. Experimental and Theoretical Phonon Frequencies. We provide a tentative assignment of bands appearing in the IR and Raman spectra of AgF_2 (wavenumbers in cm^{-1}). We classify the modes as shoulder (sh), very strong (vs), strong(s), medium (m) and weak (w). *Intensity of this band clearly grows with the illumination time; the nature of chemical species which is the product of photochemical decomposition will be elucidated elsewhere.

References

1. Emery VJ (1987) Theory of high-Tc superconductivity in oxides. *Phys. Rev. Lett.* 58(26):2794–2797.
2. Fischer P, Roult G, Schwarzenbach D (1971) Crystal and magnetic structure of silver difluoride-II. Weak 4d-ferromagnetism of AgF_2. *J. Phys. Chem. Solids* 32(7):1641–1647.
3. Slater JC, Koster GF (1954) Simplified LCAO method for the periodic potential problem. *Phys. Rev.* 94(6):1498–1524.
4. Yang X, Su H (2014) Cuprate-like electronic properties in superlattices with $Ag(II)F_2$ square sheet. *Sci. Rep.* 4:5420.
5. Yang X, Su H (2015) Electronic Properties of Fluoride and Half–fluoride Superlattices $KZnF_3/KAgF_3$ and $SrTiO_3/KAgF_3$. *Sci. Rep.* 5(1):15849.
6. Andersen OK, Klose W, Nohl H (1978) Electronic structure of Chevrel-phase high-critical-field superconductors. *Phys. Rev. B* 17(3):1209–1237.
7. Marzari N, Mostofi Aa, Yates JR, Souza I, Vanderbilt D (2012) Maximally localized Wannier functions: Theory and applications. *Rev. Mod. Phys.* 84(4):1419–1475.
8. McMahan AK, Annett JF, Martin RM (1990) Cuprate parameters from numerical Wannier functions. *Phys. Rev. B* 42(10):6268–6282.
9. De Boer DKG, Haas C, Sawatzky GA (1984) Exciton satellites in photoelectron spectra. *Phys. Rev. B* 29(8):4401–4419.
10. Ghijsen J, et al. (1988) Electronic structure of Cu_2O and CuO. *Phys. Rev. B* 38(16):11322–11330.
11. Tjeng LH, et al. (1990) Electronic structure of Ag_2O. *Phys. Rev. B* 41(5):3190–3199.
12. van den Brink J, Meinders M, Lorenzana J, Eder R, Sawatzky GA (1995) New Phases in an Extended Hubbard Model Explicitly Including Atomic Polarizabilities. *Phys. Rev. Lett.* 75:4658.
13. Tessman JR, Kahn AH, Shockley W (1953) Electronic Polarizabilities of Ions in Crystals. *Phys. Rev.* 92(4):890–895.
14. Cini M (1976) Density of states of two interacting holes in a solid. *Solid State Commun.* 20(6):605–607.
15. Sawatzky GA (1977) Quasiatomic auger spectra in narrow-band metals. *Phys. Rev. Lett.* 39(8):504–507.
16. Antonides E, Janse EC, Sawatzky GA (1977) LMM Auger spectra of Cu, Zn, Ga, and Ge. I. Transition probabilities, term splittings, and effective Coulomb interaction. *Phys. Rev. B* 15(4):1669–1679.
17. Powell CJ (1978) Solid-state features in the valence band Auger spectra of copper, silver and gold. *Solid State Commun.* 26:557–562.
18. Parry-Jones AC, Weightman P, Andrews PT (1979) The M4,5N4,5N4,5 Auger spectra of Ag, Cd, In and Sn. *J. Phys. C Solid State Phys.* 12(8):1587–1600.
19. Anderson P (1950) Antiferromagnetism. Theory of superexchange interaction. *Phys. Rev.* 79(2):350–356.
20. Braden M, et al. (1996) Structural analysis of $CuGeO_3$: Relation between nuclear structure and magnetic interaction. *Phys. Rev. B* 54(2):1105–1116.
21. Stechel EB, Jennison DR (1988) Electronic structure of CuO_2 sheets and spin-driven high-Tc superconductivity. *Phys. Rev. B* 38(7):4632–4659.
22. Martin RL, Illas F (1997) Antiferromagnetic Exchange Interactions from Hybrid Density Functional Theory. *Phys. Rev. Lett.B* 79(4):1539–42.
23. Liechtenstein AI, Katsnelson MI, Antropov VP, Gubanov VA (1987) Local spin density functional approach to the theory of exchange interactions in ferromagnetic metals and alloys. *J. Magn. Magn. Mater.* 67(1):65–74.
24. Korotin DM, Mazurenko VV, Anisimov VI, Streltsov SV (2014) Calculation of the exchange constants of the Heisenberg model in the plane-wave based methods using the Green's function approach. *Phys. Rev. B* 91:224405.
25. Sengupta P, Sandvik AW, Singh RRP (2003) Specific heat of quasi-two-dimensional antiferromagnetic Heisenberg models with varying interplanar couplings. *Phys. Rev. B* 68(9):094423.
26. Lorenzana J, Eroles J, Sorella S (1999) Does the Heisenberg Model Describe the Multimagnon Spin Dynamics in Antiferromagnetic CuO Layers? *Phys. Rev. Lett.* 83(24):5122–5125.
27. Kurzydłowski D (2013) Ph.D. thesis (Univ. of Warsaw, Poland).
28. Banks MG, et al. (2009) Magnetic ordering in the frustrated Heisenberg chain system cupric chloride $CuCl_2$. *Phys. Rev. B - Condens. Matter Mater. Phys.* 80(2).
29. Hassan A, et al. (2000) Ultrawide Band Multifrequency High-Field EMR Technique: A Methodology for Increasing Spectroscopic Information. *J. Magn. Reson.* 142(2):300–312.
30. Simon P, et al. (1993) Absence of Cu^{2+} electron-spin resonance in high-temperature superconductors and related insulators up to 1150 K. *Phys. Rev. B* 48(6):4216–4218.
31. Toth S, Lake B (2015) Linear spin wave theory for single-Q incommensurate magnetic structures. *J. Phys. Condens. Matter* 27(111):166002.
32. Walters AC, et al. (2009) Effect of covalent bonding on magnetism and the missing neutron intensity in copper oxide compounds. *Nat. Phys.* 5(12):867–872.
33. Brown J (2003) Magnetic Form Factors in *Neutron data Bookl.*, eds. Dianoux AJ, Lander GH, Institut Laue-Langevin. (Old City Publishing Group, Philadelphia).